Eng. Sci., 2025, **38**, 1922

Engineered Science
DOI: https://dx.doi.org/10.30919/es1922

High-Fidelity Distributed Brillouin Sensing with Optical Mechanisms Fusion and Data Transfer

Yongxi He,* Ye Liang, Wenjie Gao, Xuechao Duan* and Yongqiang Guan

Abstract

Distributed optical fiber Brillouin sensing has the unique ability of long-distance and high spatial resolution measurement, offering substantial potential across multiple fields. However, compared with point-based strain sensing techniques, the accuracy of high-resolution Brillouin strain measurements remains limited, due to challenges such as nonlinear scattering, low signal-to-noise ratio, and gain spectrum fitting error. Here we proposed and demonstrated the optically fused mechanism of Brillouin strain and Bragg grating strain in the same fiber, and developed a new transfer model for fidelity enhancement of distributed strain based on their high level of similitude. This transfer model combined affine transformation with adaptive weighting to effectively map strain instance vectors with large data gaps and significant dimension differences. For a 2.5-km precision fiber-optic coil used in underwater autonomous underwater vehicle (AUV) navigation, the average measurement error significantly decreased by 79% from 10.5% to 2.2% within 34.8 s compared to that before transfer. Only a small amount of reliable strain data was needed to improve the fidelity level of the distributed strain for each measurement. The sensing approach offers high accuracy, non-destructiveness, simple wiring, and low cost, making it suitable for long-distance underwater communication, geological disaster early warning, and aerospace structural fatigue monitoring.

Keywords: Distributed sensing; Nonlinear error; Optical fusion; Data transfer; Structural assessment.
Received: 03 October 2025; Revised: 28 November 2025; Accepted: 04 December 2025
Article type: Research article.

1. Introduction

Autonomous underwater vehicles (AUVs) serve as vital instruments for exploring the rich mineral, biological and genetic resources contained in the deep-sea environment. The two-way high-speed communication link between the AUV and the ground control center is crucial for real-time control and data transmission.[1-3] Compared to the electromagnetic or acoustic communication, optical fiber communication offers significant advantages, including immunity to surrounding interference, cross-media transmission capability, long-distance signal propagation, and high-capacity information transfer[4-6] (Fig. 1). Kilometers of fine optical fibers (Diameter: ~0.3 mm) are precisely pre-wound into optical fiber coils and passively deployed layer by layer during AUV navigation to establish long-distance and variable-length communication pathways.[7,8] The wound optical fiber coil needs to be preliminary evaluated in the release safety based on initial strain before installation on AUV. Obtaining accurate initial strain distribution within the optical fiber coil at high fidelity and high spatial resolution (~10 cm) is a prerequisite for evaluating these precise structures.[9]

Fiber Bragg grating (FBG) sensors have been widely used for structural strain measurements, featuring high measurement sensitivity and accuracy with a minimum static resolution of 270 pε.[10] Only a limited number of discrete strain measurements can be obtained along an optical fiber utilizing wavelength division multiplexing due to the limitation of spectral bandwidth. As an alternative, distributed optical fiber sensors have received widespread attention for long-distance measurements, such as optical time domain reflectometry (OTDR) and Brillouin optical time domain analysis (BOTDA).[11,12] These methods rely on optical scattering effects (Rayleigh and Brillouin scattering) to achieve distributed measurements along the entire fiber and have been widely employed in the field of structural health monitoring.[13] OTDR technology employs the Rayleigh scattering mechanism to quantify transmission attenuation along the optical fiber, which is primarily for detecting,

State Key Laboratory of Electromechanical Coupling, Xidian University, Xi'an, 710071, China
**Email:* heyongxi@xidian.edu.cn (Y. He),
xchduan@xidian.edu.cn (X. Duan)

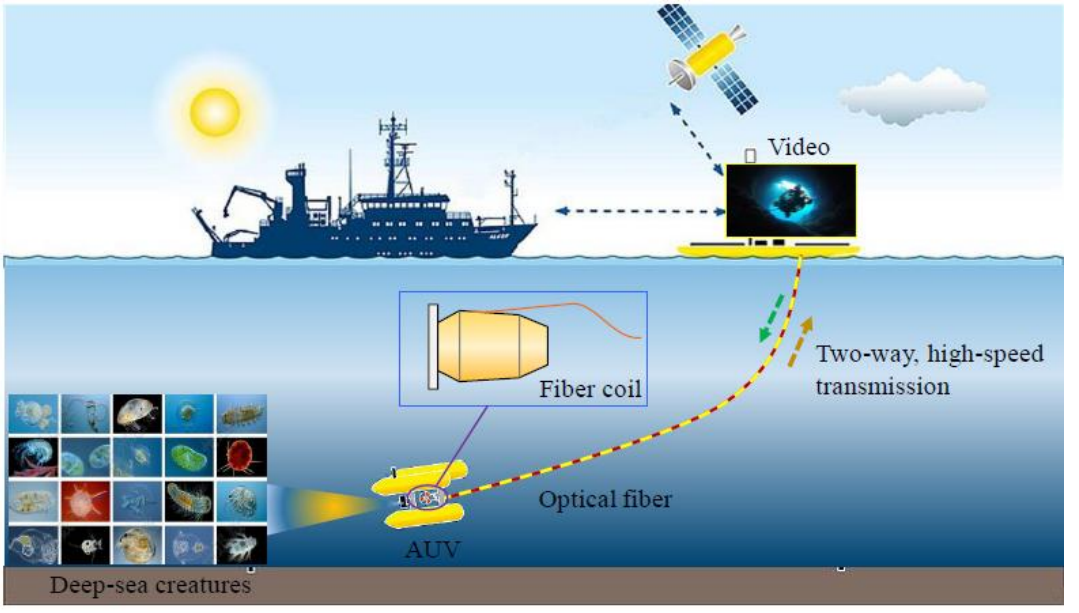

Fig. 1: Schematic diagram of establishing a long-distance underwater communication path with optical fibers.

localizing, and qualifying various fiber optic link events induced by breaks, splices, and connectors.[14] BOTDA technology employs the stimulated Brillouin scattering (SBS) mechanism to quantify distributed strain and temperature, which has demonstrated significant advantages in structural safety evaluation and health monitoring.[15] Constrained by the phonon lifetime, the pulse width cannot be reduced below 10 ns, presenting challenges in achieving spatial resolution below 1 m for a conventional BOTDA system. Bao *et al*. proposed a differential pulse-width pair (DPP) BOTDA scheme for centimeter spatial resolution by subtracting the time-domain curves generated by two long pulses, overcoming the limitations imposed by a single pulse width.[16,17] However, the attenuation of the pulse signal weakened the Brillouin gain effect, which in turn reduced the accuracy of the frequency shift measurement. Compared to the point sensing of FBG, DPP-BOTDA exhibited relatively low measurement fidelity due to the nonlinear scattering effects, low signal-to-noise ratio (SNR), and inaccuracies in gain spectrum fitting,[12,18] For high-precision structures such as communication coils and seismic hazard prediction devices, the low fidelity of the distributed strain was prone to cause serious security prediction mistakes.

Multi-source data fusion techniques have demonstrated to be very efficient tools to improve data accuracy.[19-21] Jin *et al*. measured the strains for the same target using distributed sensors and multiple point sensors, and improved the accuracy of distributed data by introducing input-connected Gaussian process mapping to complementarily fuse point and distributed data.[22] A large number of discrete point sensors also needed to be deployed across the structural surface, rendering this method unsuitable for application in wound optical fiber coils. In the hybrid measurement of BOTDA and FBG, Zhang *et al*.[23] and Zrelli *et al*.[24] proposed hybrid BOTDA and FBG system for multi-parameters measurement in complex conditions, the sensing mechanisms of which were physically independent. Zhou *et al*.[25] attempted to combine distributed Brillouin and local FBG sensors on one single-mode optical fiber, and investigated the coupling characteristics between FBGs and Brillouin signals from an experimental point of view. The results indicated that the FBG signal introduced evident signal distortion to the BOTDA power spectrum near the grating region, and Zhou *et al* further used wavelet de-noising algorithm to fit the Brillouin frequency shift. He *et al*. proposed a Long Short-Term Memory (LSTM) model for strain error compensation of BOTDA sensing based on a large number of data memory.[26] The method relied on a large number of labeled data for model training and was just applicable to specific types of measurement structures. In distributed sensing systems, data measured with a single scattering mechanism have limited accuracy and cannot reflect the practical strain state within a precise structure. Combining FBGs and BOTDA mechanisms into the same fiber can provide a potential combination of the sensing advantages of point and distributed strain sensors. To date, little reports have demonstrated a high-fidelity strain sensor network at high fidelity and high spatial resolution for the inner sensing of precise optical fiber structures.

The goal of this study was to optically integrate the FBG sensing mechanism with the BOTDA sensing mechanism in the same optical path and perform simultaneous measurements, as shown in Fig. 2. Although some disparity was observed in

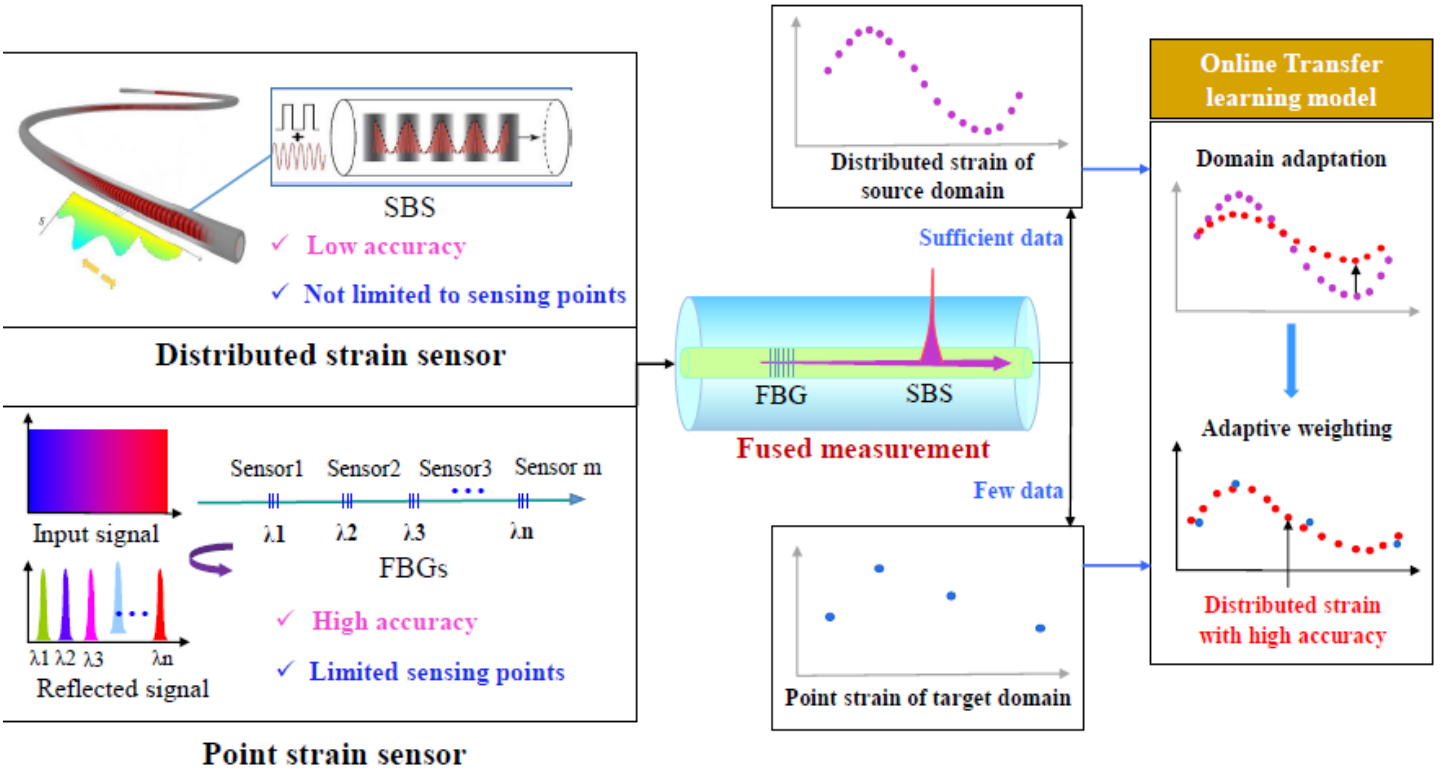

Fig. 2: Fidelity enhancement of distributed Brillouin strain sensing with optical mechanisms fusion and data transfer.

the two sets of strains, the data distribution laws were similar for the same object. When the distributed strain law was transferred to the accurate point strains, the resulting strains took advantages of both mechanisms, and a higher accuracy was theoretically obtained. Based on this concept, the strain data measured by BOTDA were de-noised as the source domain and the FBGs strain data were used as target domain. In this application scenario, the source and target domains not only varied from each measurement, but also the transfer relationship varied from optical fiber coils. Off-line transfer learning relied on static source and target domain data. If it needed to adapt to new data, model re-training was required,[27] which was struggled to adapt to the dynamically changing source and target domains. An online transfer learning-based method was proposed to enhance the fidelity of distributed strain by transferring the Brillouin strain to discrete FBG strain. If the source domain and target domain had large data gaps and significant size differences, traditional transfer learning algorithms were difficult to obtain an acceptable transfer effect.[28] This work further presented a new transfer learning algorithm to enhance the fidelity of distributed strain by integrating domain adaptation using affine transformation and adaptive weighting. For each measurement of the distributed strain, only a few accurate data points were required to online transfer the distributed strain from low fidelity to high fidelity.

The remainder of this paper was organized as follows: Section 2 provided details on the principle for the optically fusing of BOTDA and FBGs in the same fiber. Section 3 described the problem specification and introduced the proposed online transfer learning model for enhancing the fidelity of distributed strain. Section 4 provided two detailed cases to validate the accuracy of the fidelity enhancing model.

2. Optical fusion principle for BOTDA and FBG

In the BOTDA system, pulsed pump light and continuous probe light are injected into the fiber under test (FUT) in opposite propagation direction. A laser with a frequency v_p is intensity-modulated to produce pulsed light, which is emitted into the FUT in the +z direction, as shown in Fig. 3. The other tunable laser outputs a continuous probe light with a frequency v_s (v_s<v_p), which is emitted into the fiber in the -z direction. When the frequency difference between the pulsed and continuous light is close to the Brillouin frequency shift of the optical fiber, SBS occurs within the positions corresponding to the pulse width, and part of energy of the pump light is transferred to the probe light.

Brillouin scattering is a type of nonlinear scattering caused by acoustic phonons in optical fibers.[29] The effective refractive index and acoustic velocity change with temperature or stress, resulting in a Brillouin frequency shift. In a single-mode fiber, only backward SBS occurs and the Brillouin shift is expressed as follows:[30]

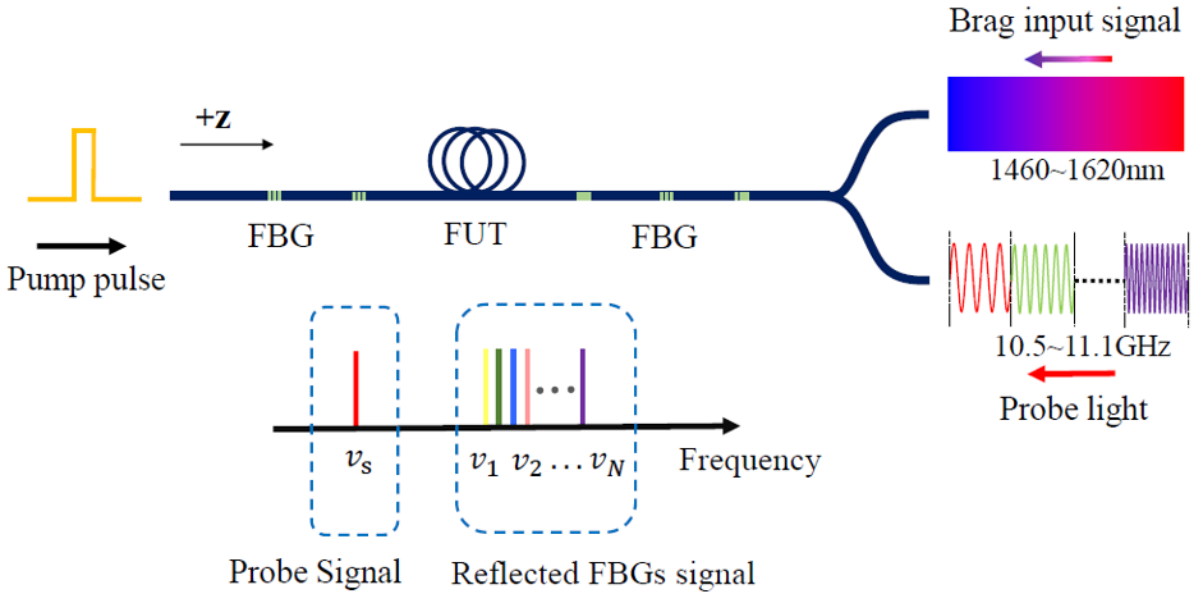

Fig. 3: Optical fusion principle for BOTDA and FBGs measurement mechanisms in the same FUT.

$$v_B = \frac{2nV_a}{\lambda_p} \tag{1}$$

where n is the effective refractive index of the fiber, λ_p is the wavelength of the pump light and V_a is the acoustic velocity in the fiber and defined as follows:

$$V_a = \sqrt{\frac{(1-k)E}{(1+k)(1-2k)\rho}} \tag{2}$$

where k is Poisson's ratio, E is Young's modulus and ρ is the fiber density.

If the refractive index n, Young's modulus E, Poisson's ratio $k$and density ρ as a function of temperature T and strain ε are denoted as $n(\varepsilon,T)$, $E(\varepsilon,T)$, $k(\varepsilon,T)$ and $\rho(\varepsilon,T)$, respectively. By combining Eqs. (1) and (2), the Brillouin frequency shift as a function of temperature and stress change is expressed as follows:

$$v_B(\varepsilon,T) = \frac{2n(\varepsilon,T)}{\lambda_p}\sqrt{\frac{[1-k(\varepsilon,T)]E(\varepsilon,T)}{(1+k(\varepsilon,T))(1-2k(\varepsilon,T))\rho(\varepsilon,T)}} \tag{3}$$

At a constant temperature T_0, the relationship between the strain and Brillouin frequency shift can be rewritten using Eq. (3) to produce the following:

$$v_B(\varepsilon,T_0) = \frac{2n(\varepsilon,T_0)}{\lambda_p}\sqrt{\frac{[1-k(\varepsilon,T_0)]E(\varepsilon,T_0)}{(1+k(\varepsilon,T_0))(1-2k(\varepsilon,T_0))\rho(\varepsilon,T_0)}} \tag{4}$$

Since the constituent SiO_2 of optical fibers has a low tensile stress, Eq. (4) is simplified by performing a Taylor series expansion and neglecting the higher-order terms:

$$v_B(\varepsilon,T_0) \approx v_B(0,T_0)[1 + \varepsilon(\Delta n_\varepsilon + \Delta k_\varepsilon + \Delta E_\varepsilon + \Delta\rho_\varepsilon)] \tag{5}$$

For $\lambda_p = 1550nm$ and temperature T =20 °C, the strain coefficients are Δn_ε =-0.22, Δk_ε =1.49, ΔE_ε =2.88, and $\Delta\rho_\varepsilon$=0.33. The relationship between the Brillouin frequency shift and the strain change is as follows in Eq. (6):[31]

$$v_B(\varepsilon,T_0) \approx v_B(0,T_0)[1 + 4.48(\varepsilon - \varepsilon_0)] \tag{6}$$

where ε_0 is the reference strain. The Brillouin frequency shift is approximately proportional to the applied strain with a coefficient of 4.48 MHz/%. Similarly, for $\lambda_p = 1550$ nm, the Brillouin frequency shift is also proportional to the temperature change with a coefficient of 1.18 MHz/°C. Considering that the temperature difference within the fiber coil is small, here we mainly focus on the strain in the fiber.

The introduction of FBG point sensors into FUT primarily results in a change in the refractive index of the fiber core at specific locations. An FBG has a constant grating period and refractive index modulation depth. The refractive index modulation distribution of a grating is sinusoidal and uniform, as given in Eq. (7):[32]

$$n_1(z) = n + \Delta n\cos\left(\frac{2\pi}{\Lambda}z\right), \quad \left(-\frac{L}{2<z<\frac{L}{2}}\right) \tag{7}$$

where $n_1(z)$ is refractive index of the fiber core at grating, Δn is refractive index modulation depth, Λ is grating period and L is grating length. Whether FBGs have an impact on the distributed strain data is discussed from the perspective of the refractive index. According to Eq. (5), the strain-induced Brillouin frequency shift at the location of an FBG is expressed as follows in Eq. (8):

$$v_B(\varepsilon,T_0) \approx v_B(0,T_0)\left[1 + \varepsilon\left(\Delta n_\varepsilon + \Delta n\cos\left(\frac{2\pi}{\Lambda}\right)z + \Delta k_\varepsilon + \Delta E_\varepsilon + \Delta\rho_\varepsilon\right)\right] \tag{8}$$

If the refractive index modulation depth $\Delta n \cos\left(\frac{2\pi}{\Lambda}\right) z$ at the grating position is much smaller than the coefficient of strain-induced refractive index change Δn_ε =-0.22, the modulation of refractive index at the FBG does not induce an evident Brillouin frequency shift. To avoid mutual strain interference in the dual-mechanism fused system, FBGs are fabricated based on the ultraviolet (UV) photosensitivity of doped optical fibers, since the refractive index reaches a saturation state with only a 10^{-4} increase in single-mode fibers.[33] This interference is almost negligible compared to the strain-induced refractive index change Δn_ε.

BOTDA is a two-end input measurement, while FBG is a single-end input measurement. There are two configurations for signal input and transmission. As shown in Fig. 3, in the first configuration, the Bragg input signal (1460~1620 nm) and Brillouin probe light (10.5~11.1 GHz) are emitted into the fiber at the same end in the $-z$ direction, while pump light is emitted from the other end. The probe light can pass through a set of discretely distributed FBGs and reach the other end for Brillouin strain demodulation due to the significant frequency difference of probe light and the central wavelength of gratings. The continuous light reflected from FBGs and pump pulse are along the $+z$direction, and its total power is detected at the emitting end of the Bragg input signal. Due to the difference in the forms of continuous light and pump light, distinct FBG center-wavelength reflection peaks in the power spectrum will be observed; and thus, the strain at FBGs can be demodulated.

In the second configuration, the pump light and Brag input signals are emitted into the fiber in the $-z$ direction, while probe light is emitted from the other end. The continuous light reflected from FBGs and the continuous probe light have the same propagation direction. The weak light power reflected from FBGs will be submerged into the high-power probe light, and the FBGs strain is difficult to demodulate. Therefore, in addition to refractive index modulation depth, another factor for the simultaneous Brillouin and FBGs strain demodulation is to ensure that the propagation direction of the continuous probe light is opposite to the direction of the backscattered light from the FBGs.

3. Online transfer learning model for enhancement of the strain fidelity

3.1 Problem specification

Machine learning algorithms can train accurate prediction models with sufficient training data. However, in many practical applications, data labeling is expensive and time-consuming.[34] The concept behind transfer learning is to transfer the existing data distribution laws from the source domain to the target domain, to train a data model suitable for the target domain. The distributed Brillouin strain has already reflected the strain distribution law in the FUT, and transferring it to the point FBGs strain will result in a relatively accurate distributed strain. In this study, a fidelity enhancing method for distributed strain with transfer learning is proposed. For each measurement, only a small amount of reliable strain data is needed to improve the fidelity level of the distributed strain, without the need for a large amount of labeled data to establish complex implicit correlations between the distributed and point strains.

The fused optical system of BOTDA and FBGs is used to simultaneously obtain the distributed and point strain for the FUT, and they are set as source domain and target domain, respectively. Online training is then conducted on the correlation between the source domain and target domain by integrating the domain adaptation and adaptive weighting.

The notation and definitions used in this paper are as follows:

$\boldsymbol{X}_{sou}$ denotes the distributed strain space of the whole precise structure, namely, the low-fidelity data measured by BOTDA, which is defined as the source domain. The positions within the structure are marked along the length of the optical fiber. For a strain instance at any point $\boldsymbol{x}_i$, $\boldsymbol{x_i} = \{p_{1i}, \varepsilon_{1i}\}$, $\boldsymbol{x}_i \in \boldsymbol{X}_{sou}\ (i = 1,2,\dots,n)$, where p_{1i} and ε_{1i} denote the position and strain of the i measurement point, respectively.

$\boldsymbol{Y}_{tar}$ denotes the discrete strain space of the whole precise structure, namely, the high-fidelity data measured by FBGs, which is defined as the target domain. For a strain instance at any measurement point $\boldsymbol{y_i} \in \boldsymbol{Y_{tar}}\ \ (i = 1,2,\dots,m)$, $\boldsymbol{y_i} = \{p_{2i}, \varepsilon_{2i}\}$, where p_{2i} and ε_{2i} denote the position and corresponding strain of the i grating, respectively.

The goal is to learn a model of $\boldsymbol{f_T}(\boldsymbol{x_i})$ mapping instance vectors from space $\boldsymbol{X}_{sou}$ to space $\boldsymbol{Y}_{tar}$ such that the distribution laws of the source domain can be transferred to the target domain. The size of $\boldsymbol{Y}_{tar}$ is usually much smaller than $\boldsymbol{X}_{sou}$. Therefore, we need to consider how to train $\boldsymbol{f_T}(\boldsymbol{x_i})$ to establish the mapping relationship for arbitrary $\boldsymbol{X}_{sou}$ and $\boldsymbol{Y}_{tar}$. Furthermore, the correlations between the two domains vary across different strain distributions. After each strain measurement, both $\boldsymbol{X}_{sou}$ and $\boldsymbol{Y}_{tar}$ are used as training data to establish an online transfer model between the two domains; thus, this process quickly transforms the inaccurately distributed data into high-fidelity data.

3.2 Online transfer learning-based fidelity enhancing model

3.2.1 Domain adaptation with affine transformation

A new transfer learning model was proposed that combines affine transformation and adaptive weighting to address the challenge of mapping strain instance vectors between the source domain and target domain with large data gaps and significant size differences. First, domain adaptation based on affine transformations is designed to globally narrow the gap between the two domains. Affine transformations involve translation, rotation and scaling. By defining the affine matrix as $\boldsymbol{W}$ and the transformed data as $\boldsymbol{X}_{sou}\boldsymbol{W}$, the goal of the affine transformation is to minimize the distance between $\boldsymbol{X}_{sou}\boldsymbol{W}$ and $\boldsymbol{Y}_{tar}$:

$$min|\boldsymbol{X}_{sou}\boldsymbol{W}-\boldsymbol{Y}_{tar}| \quad (9)$$

where

$\boldsymbol{X}_{sou}\in R^{n\times 3}$, $\boldsymbol{Y}_{sou}\in R^{m\times 3}$, $\boldsymbol{X}_{sou}=\begin{bmatrix}P_{11} & \varepsilon_{11} & 1\\ \vdots & \vdots & \vdots\\ P_{1n} & \varepsilon_{1n} & 1\end{bmatrix}$, and $\boldsymbol{Y}_{tar}=\begin{bmatrix}P_{21} & \varepsilon_{21} & 1\\ \vdots & \vdots & \vdots\\ P_{2m} & \varepsilon_{2m} & 1\end{bmatrix}$.

Eq. (9) is difficult to calculate because the size of $\boldsymbol{X}_{sou}$ is not equal to $\boldsymbol{Y}_{tar}$, $n\neq m$. The strains in the source domain at FBGs positions are extracted as a new domain $\boldsymbol{X}_{sou\_1}$. When $\boldsymbol{X}_{sou\_1}$ and $\boldsymbol{Y}_{tar}$ have the same size, Eq. (9) is transformed into the following Eq. (10):

$$min\left|\boldsymbol{X}_{sou\_1}\boldsymbol{W}-\boldsymbol{Y}_{tar}\right| \quad (10)$$

This is a typical least squares linear regression problem and the solution of the affine matrix $\boldsymbol{W}$ is represented as follows in Eq. (11):

$$\boldsymbol{W}=\left(\boldsymbol{X}_{\text{sou\_1}}{}^{T}\boldsymbol{X}_{\text{sou\_1}}\right)^{-1}\boldsymbol{X}_{\text{sou\_1}}{}^{T}\boldsymbol{A} \quad (11)$$

where

$$\boldsymbol{X}_{sou\_1}=\begin{bmatrix}P_{21} & \varepsilon_{11} & 1\\ \vdots & \vdots & \vdots\\ P_{2m} & \varepsilon_{1m} & 1\end{bmatrix},\ \boldsymbol{A}=\begin{bmatrix}\varepsilon_{21}\\ \vdots\\ \varepsilon_{2m}\end{bmatrix}.$$

Then, $\boldsymbol{X}_{sou}$ is transferred to $\boldsymbol{X}'_{sou}$, as follows Eq. (12):

$$\boldsymbol{X}'_{sou}=[p_{1i},X_{sou}W] \quad (12)$$

After domain adaptation, the distributions of $\boldsymbol{X}'_{sou}$ and $\boldsymbol{Y}_{tar}$ are macroscopically close to each other, and this process is denoted as $\boldsymbol{f}_1(\boldsymbol{x_i})$.

3.2.2 Weight-adaptive regression

With domains $\boldsymbol{X}'_{sou}$ and $\boldsymbol{Y}_{tar}$, the direct correlation model $\boldsymbol{f}_2(\boldsymbol{x_i})$ is further trained to establish the mapping relationships of the strain instance vectors. Adaptive weighting controls the contributions of each point strain to the correlation model, ensuring that the $\boldsymbol{X}'_{sou}$ curve is locally adjusted to be as close as possible to $\boldsymbol{Y}_{tar}$. Considering its stability in dynamically adjusting sample weights and fast convergence efficiency, the adaptive weighting algorithm TrAdaBoost.R2[35] is used to establish the correlation model $\boldsymbol{f}_2(\boldsymbol{x_i})$.

$\boldsymbol{X}'_{sou}$and $\boldsymbol{Y}_{tar}$ are combined to form the training space, $\boldsymbol{Z}$: as shown in Eq. (13)

$$\boldsymbol{Z}=\boldsymbol{X}_{sou}\cup\boldsymbol{Y}_{tar}:\ \boldsymbol{Z}=\{(P_i,\varepsilon_i)\}\ \text{where}\ p_i=\begin{cases}p_{1i},\ i=1,\cdots,n\\ p_{2i},\ i=n+1,\cdots,n+m\end{cases} \quad (13)$$

The function of TrAdaBoost.R2 is to increase the weight of target strain during the training process, thus enhancing their impact on the correlation model. At the half distance range of each p_{2i}, the strain influence of target domain to that of source domain is the same. Initially, the weights of all the training data are set to the same value and the initial weight vector is defined as follows in Eq. (14):

$$\boldsymbol{w}_i^1=\frac{1}{n+m},\ i=1,\cdots,n+m \quad (14)$$

The basic decision tree regressor is used as an iterative base learner considering its low sensitivity to noise and outliers.[36] The prediction function is defined as $g_t:p_i\rightarrow\varepsilon_i$. The relative training error for each target instance is defined as follows in Eq. (15):

$$\frac{\varepsilon_i-g_t(p_i)}{\varepsilon_i}\ \text{where}\ n+1<i<n+m \quad (15)$$

when the target label is incorrectly predicted, the instance weights in $\boldsymbol{Y}_{tar}$ are adjusted to minimize the impact on $\boldsymbol{X}'_{sou}$. In new round of iteration, the weight vector is calculated based on the training error coefficients e_i^t of all data in previous round: as shown in Eq. (16)

$$e_i^t=\frac{\left\|\left(\varepsilon_i-\frac{g_t(p_i)}{\varepsilon_i}\right)\right\|}{D_t}\ \text{where}\ t=1,\cdots,N \quad (16)$$

where D_t is the maximum training error for the target training data. The details of algorithm TrAdaBoost.R2 can be found in.[35]

Therefore, the transfer model $\boldsymbol{f_T}(\boldsymbol{x_i})$ from the source domain to the target domain consists of the affine transformation $\boldsymbol{f}_1(\boldsymbol{x_i})$ and weight-adaptive regression $\boldsymbol{f}_2(\boldsymbol{x_i})$. Since the transfer parameters between the two domains are dynamically established, the fidelity enhancement of the distributed strain is accomplished after each measurement based on the online transfer learning model. This method is widely applicable when distributed instances are variable. Based on Big O notation, the time complexity of the affine transformation is $T_1=O(m\times n)$, where m and n are the size of source and target domain, respectively. The time complexity of the weight-adaptive regression is $T_2=O\big(epoch\times((m+n)\,log(m+n))\big)$, where $epoch$ is the training rounds for TrAdaBoost.R2.

4. Experiments

4.1 Experimental setup

As a verification of the proposed fusing mechanism of BOTDA and FBGs, the experimental setup was implemented, as shown in Fig. 4. Based on a fast DPP-BOTDA scheme,[16] additional broadband light for FBG measurement was coupled into the FUT along the probe light. Ultra-narrow-linewidth laser 1(LD, 3 kHz, RIO, RIO0074-4-00-3) operating at 1550 nm was split into distinct branches at 90: 10, where the 90% branch was used to generate the Brillouin pump light and the 10% branch served as the continuous probe wave. In the upper branch, an electro-optic modulator (EOM1, 35 dB, EOSPACE, AX-0S5-10-PFU-PFU) was utilized to produce the 8.335 GHz double sidebands. Then, EOM2 was driven by an arbitrary waveform generator (AWG1) to generate an optical pulse pair

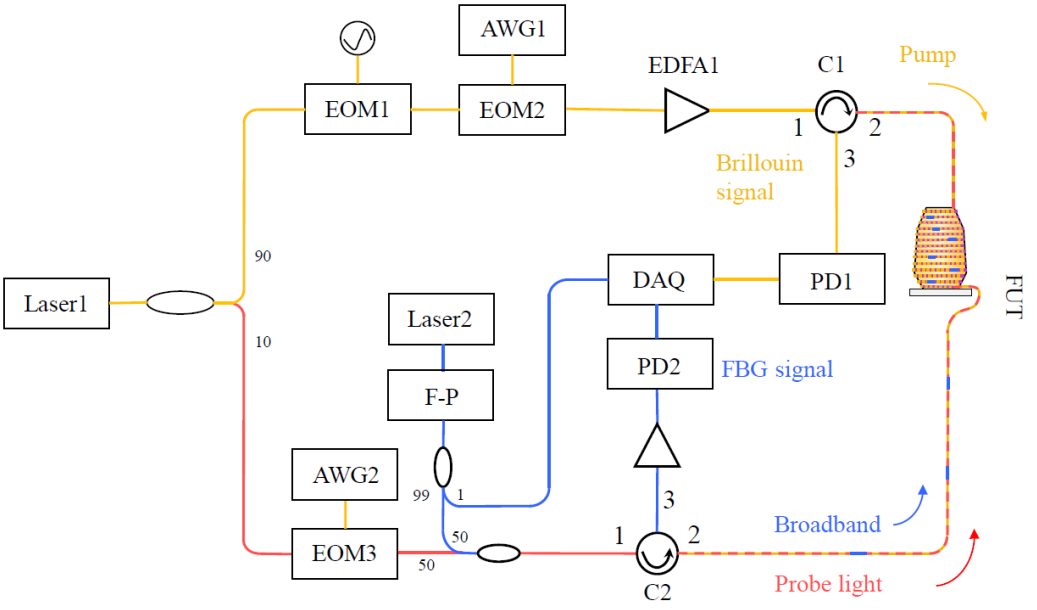

Fig. 4: Experimental setup of the dual-mechanism fused measurement system.

with the widths of 50 and 49 ns, corresponding to a 10 cm spatial resolution. Its peak power was amplified to 100 mW by the erbium-doped fiber amplifier (EDFA1, Beijing Conquer Optical Technology Company Ltd., KG-EDFA-P-17-00-M-FA), and the generated pulse was injected into the FUT through an optical circulator (C1), thus forming the pump light consisting of 50/49 ns optical pulses at 1550 nm with a peak power of 100 mW. In the lower branch, the 10% light from laser 1 was modulated by EOM3 to generate the probe light, and the driving microwave signal was provided by AWG2, sweeping from 10.5 GHz to 11.1 GHz with a frequency step of 4 MHz. At the same time, broadband laser 2 was combined with a tunable F-P filter to output light with wavelengths ranging from 1460 nm to 1620 nm at a fixed scanning interval of 200 pm, serving as the light source of FBGs and providing a wavelength-scanning Bragg input signal for FBG interrogation. 1% of the broadband light was used as a reference for the FBG signal demodulation. 99% of the broadband light and the probe light were simultaneously coupled into FUT through port 2 of C2. Thus, pump light and probe light were transmitted along the opposite direction in FUT, while the reflected broadband signal from FBGs had the opposite propagation direction with probe light.

The Brillouin signal was collected through port 3 of C1. A high-gain photodetector (PD1) with a 350 MHz bandwidth was used for Brillouin signal detection. There were several FBGs (grating length: 3 mm) with nonoverlapping center wavelengths in the FUT, except for 1550 nm. The reflected FBG signal was detected from port 3 of C2 with a PD2 at 1000 Hz, and the Bragg wavelength was determined by identifying the location of the highest light intensity. Both the Brillouin strain and FBG strain signals carried the strain information of FUT, and the output of these two PDs was simultaneously recorded by a dual-channel data acquisition (DAQ) with 1 GSa/s sampling rate.

4.2 Dual-mechanism fusion measurement

To validated the effectiveness of dual-mechanism fusion measurement, a customized optical fiber segment (Length: 1 m) containing 6 FBGs was tested under a series of strains and temperatures. The FUT was a single-mode silica fiber (Yangtze, Bl1011-A) with a core/cladding diameter of 9 μm/125 μm and an attenuation of approximately 0.2 dB/km at 1550 nm. A precision optical shifter (Huike, LX80-L) and magnetic fiber-optic clamp formed a micro-strain fine-tuning platform with a resolution of 1 μm. The FBGs were prepared by the phase mask method (Top Photonics, Noria) with a single-mode (SM) optical fiber with acylate coating (Yangtze, Bl1011-A, Core/Cladding diameter: 7.4 μm/125 μm). The space between the FBGs was 10 cm, and reflectivity was 0.1%. The central wavelengths were 1515 nm, 1524 nm, 1534 nm, 1544 nm, 1554 nm and 1565 nm, respectively. To facilitate the generation of stable Brillouin scattering, 500-meter-long optical fibers were added to both ends of the fiber segment. The test strain was applied up to ~1000 uε where acylate coating was prone to broken at the clamp position beyond larger strain. The test temperature was applied to the upper limit of optical fiber's operating temperature of 85 °C by water bath. Brillouin strain (temperature) and FBG strain (temperature) were simultaneously obtained by the dual-mechanism fused strain measurement system. The working feasibility of dual-mechanism fusion was assessed according to whether the signal noise and strain/temperature changes were observed beyond the fiber segment. The sensitivity and accuracy of the Brillouin strain were evaluated with the average strain measured by FBGs as a reference.

4.3 Accuracy validation for the fidelity enhancing model

The accuracy of the transfer learning-based fidelity enhancing model was validated using two practical cases: a wound fiber-optic gyro with a length of 30 m (referred to as Coil-30) and a

precise fiber coil with a length of 2.5 km for underwater AUV navigation guidance (referred to as Coil-2500). Both were fabricated from the same batch of single-mode optical fiber as the customized optical fiber segment described in Section 4.2, ensuring consistent fiber properties across all experiments. These conditions corresponded to the short-range, low-strain conditions and the long-range, complex-strain conditions, respectively. A portion of FBGs strain served as the target domain while the remaining FBGs strain served as the validation domain. The accuracy of the distributed strain was assessed by comparing distributed strain curve after transferring to the FBG strains in the validation domain. A comprehensive cross-validation method was conducted by replacing the target domain three times for each measurement, which allowed more FBG strains to participate in the accuracy validation and better reflected the fidelity enhancing effect. Three validation domains were set as $\boldsymbol{Y}_{tar-1}$, $\boldsymbol{Y}_{tar-2}$ and $\boldsymbol{Y}_{tar-3}$, respectively. The average measurement error Er was used to evaluate the accuracy of the Brillouin strain for a structure and was defined as the arithmetic mean of the relative measurement errors in the validation domain, as follows in Eq. (17):

$$Er = \frac{1}{M}\sum_{i=1}^{M}\left|\frac{\varepsilon_{i_{transfer}} - \varepsilon_{i_{FBGV}}}{\varepsilon_{i_{FBGV}}}\right| \times 100\% \qquad (17)$$

where $\varepsilon_{i_{FBGV}}$ was the i^{th} FBG strain in the validation domain, $\varepsilon_{i_{transfer}}$ was the Brillouin strain after transferring at the same position of the i^{th} FBG and M was the size of validation domain.

The fiber-optic gyro Coil-30 was a precise component for the angular velocity sensing in inertial attitude system, consisting of a wound optical fiber cable on a spool with a diameter of 10 cm. The single-mode optical fiber (Yangtze, Bl1011-A) with a glass fiber reinforced jacket (diameter: 0.32 mm) was used in both cases. 22 FBGs were prepared before jacketing with initial central wavelength ranging from 1520 nm to 1585 nm at an interval of 3 nm. The Brillouin strain with 600 measurement points was denoised with the Savitzky-Golay method and then set as the source domain. 11 evenly distributed FBGs were used as the target domain and the remaining 11 FBGs were used as the validation domains. The fiber Coil-2500 was a crucial component that established communication between the underwater AUV and ground-based control centers. The optical fiber cable was tightly wound layer by layer in the form of a helix around a composite core tube. The winding was reversed across two turns to start the next layer of winding. The resulting fiber coil in this structure had 10 layers. There were 50000 measurement points for Brillouin strain. The key features of abrupt strain changes at the layer crossing positions were preserved using a thresholding filter, while the remaining data were denoised using the Savitzky-Golay method and subsequently designated as the source domain. 55 FBGs were prepared before jacketing and they were evenly distributed in each layer. 35 FBGs were used as the target domain and the remaining 15 FBGs were used as the validation domains.

Affine transformation and adaptive weighting were tested independently to validate the contributions of each part in the proposed model. The parameter domain size ratio SR was further defined as the size ratio of the source domain to the target domain. With the same target domain, SR was set as 714, 357, 200, 100, 50 and 25 respectively by using equally spaced sampling strategy to study the influence of SR on fidelity enhancing. The model incremental update mechanism was introduced[37] to enhance the computational efficiency by starting each training with the weighted base learners from the pre-training (SR =25).

4.4 Comparison with existing methods

Three kinds of existing methods were chosen to demonstrate the superiority of the proposed approach in this study. Inverse distance weighting (IDW):[38] IDW was a simple weighted fusion based on spatial proximity. It assigned differentiated weights to data points at different locations through a distance attenuation function, thereby achieving weighted fusion of distributed and point strain. Gaussian process regression (GPR):[19] GPR was an advanced data-fusion method based on Gaussian process regression, which used the covariance function (kernel function) to capture the relationships of distributed and point strain. Deep Adaptation Network (DAN), Joint Adaptation Network (JAN) and Long Short-Term Memory (LSTM):[39] Three advanced deep transfer learning networks were chosen to transfer the distributed strain to point strain based on Transfer-Learning-Library provided by Tsinghua University. All of algorithms were conducted on a computer with inter-core i7-14700F@5.4GHz, 20 core-28thread.

5. Results and discussion

5.1 Dual-mechanism fusion measurement In the experiment, a 1 m fiber segment containing 6 uniformly distributed FBGs was stretched between 516 m and 517 m of the 1 km single-mode fiber. Brillouin strain and FBG strain were simultaneously obtained by the proposed dual-mechanism fused strain measurement system. As the continuous probe light and the FBG backscattered light propagated in opposite directions, the typical Brillouin strain across 0~1039.1 με range around the targeted fiber segment were shown in Fig. 5(a-f). The fiber section between 513 m and 519 m was in a relaxed state, as marked by the green dots in Fig. 5(a), where the initial Brillouin strain approached 0 με. In contrast, the initial Brillouin strain in the remaining wound fiber sections on both sides was approximately 220 με. Notably, no significant signal noise was observed around the fiber segment containing 6 FBGs, as marked by the orange dots. As the applied strain increased stepwise to 77.6 με, 313.7 με, 533.3 με, 825.9 με, and 1039.1 με, the Brillouin strain response exhibited localized increases exclusively within the segment, while strain values at all other positions remained stable, with

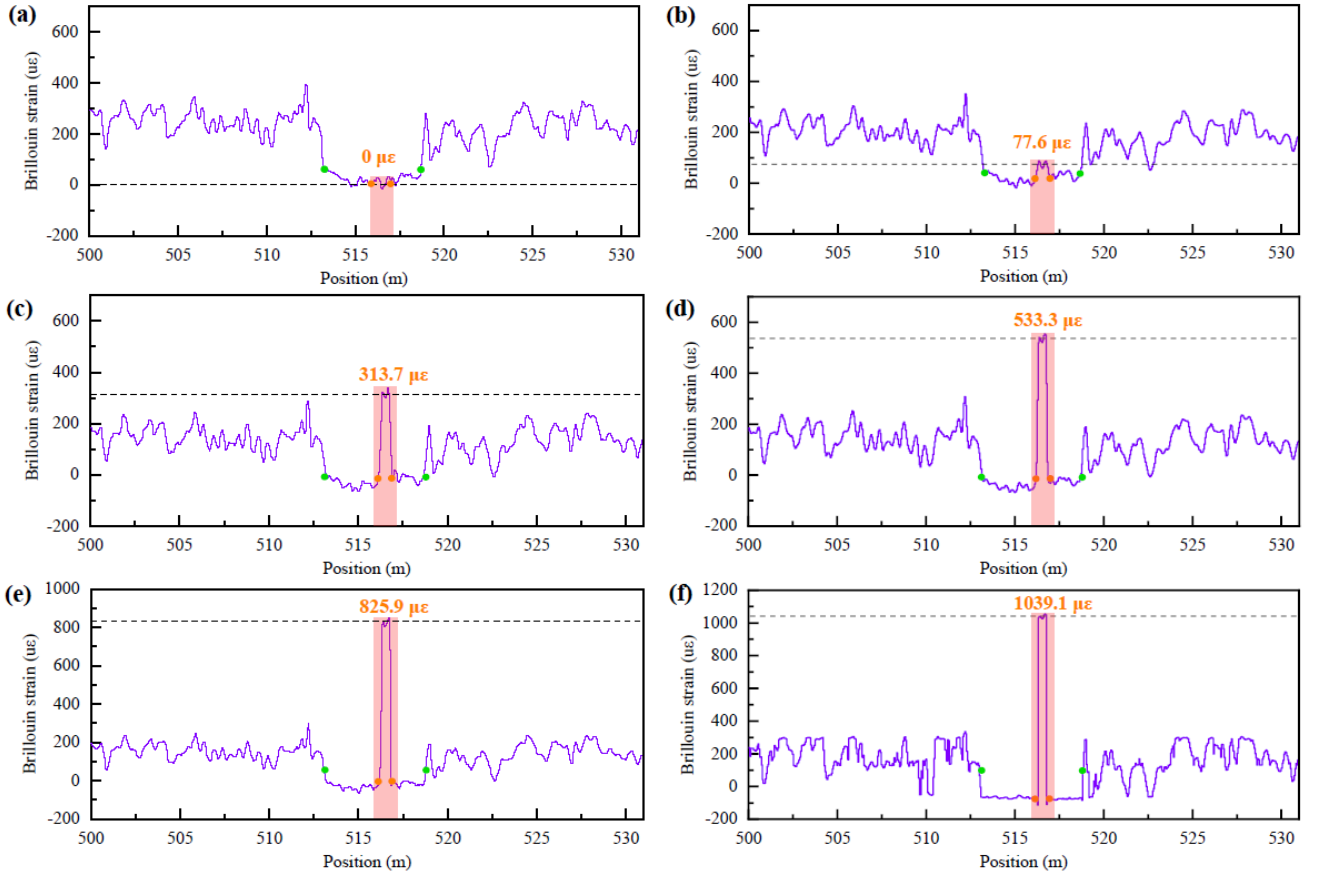

Fig. 5: Typical Brillouin strains around the fiber segment at (a) 0 με, (b) 77.6 με, (c) 313.7 με, (d) 533.3 με (e) 825.9 με and (f) 1039.1 με.

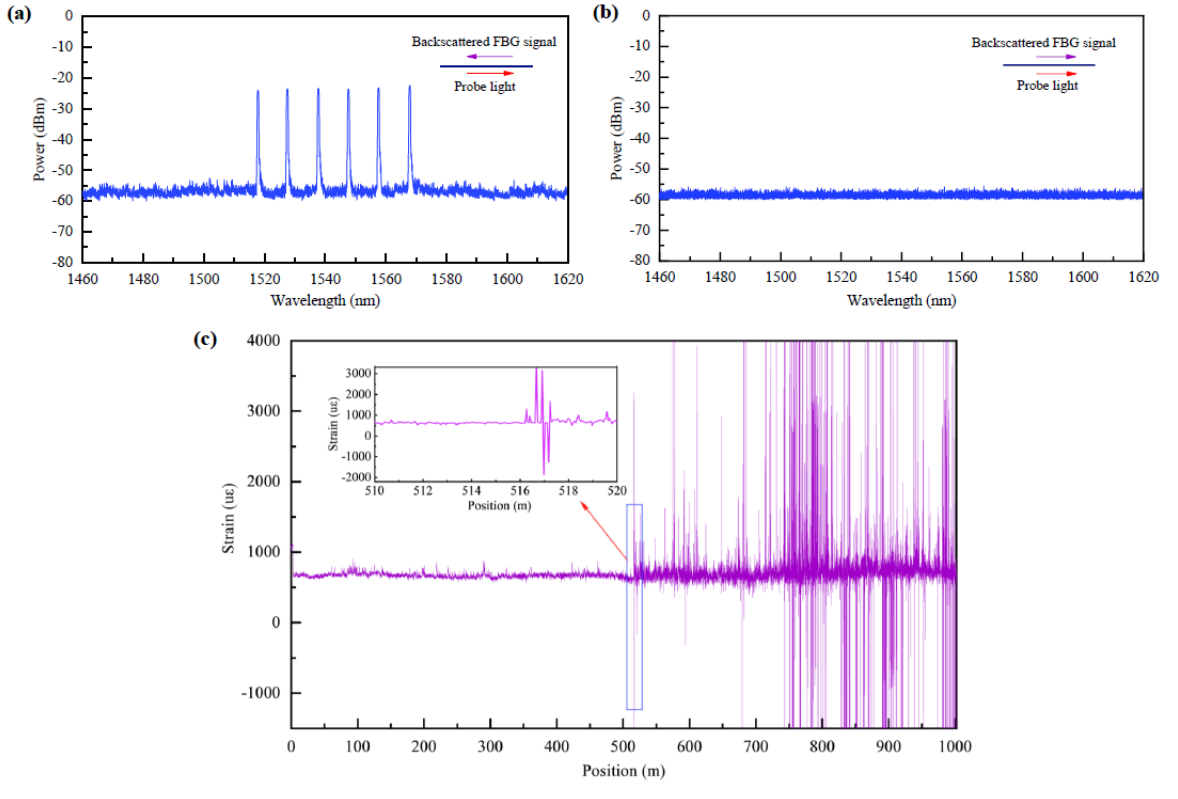

Fig. 6: Demodulated FBG spectrum with probe and backscattered light propagating in (a) opposite and (b) same directions for low-reflectivity FBGs (0.1%) fused configuration. (c) Demodulated Brillouin strains for conventional 30% reflectivity FBGs in fused configuration.

no observable signal distortion or noise generation (Fig. 5(b-f)).

The FBG spectrum was easily demodulated under this configuration from the two mixed powers due to distinct lightwave differences (Fig. 6(a)). This verified the feasibility of the optical fusion principle for BOTDA and FBG, as described in Section 2. However, when both the continuous probe light and the FBG backscattered light propagated co-directionally, the FBG signal was overwhelmed by the high-power probe light due to their identical optical characteristics, rendering the FBG spectrum undemodulatable (Fig. 6(b)). Furthermore, when the fiber segment was replaced with a conventional FBG having a reflectivity of 10%, significant signal distortion emerged from the FBG location at 516 m extending to 1000 m in the Brillouin strain profile, as shown in Fig. 6(c). Therefore, the foundation for the optical fusion of BOTDA and FBG mechanisms lies in the counter-propagation of the continuous probe light relative to the backscattered light from the FBGs. Additionally, the refractive index modulation at the FBGs did not induce any measurable Brillouin frequency shift. The fiber segment was further tested up to a temperature limit of approximately 85 °C (Fig. 7), where similar phenomena were consistently observed. These results indicate that the two sensing mechanisms operate nearly independently within the same optical fiber.

Both strain measurements were acquired simultaneously within the same optical fiber (Fig. 8(a)), with no strain fixation errors or loading inaccuracies introduced during the experiment. Although the Brillouin strain and Brillouin frequency shift are theoretically expected to exhibit an

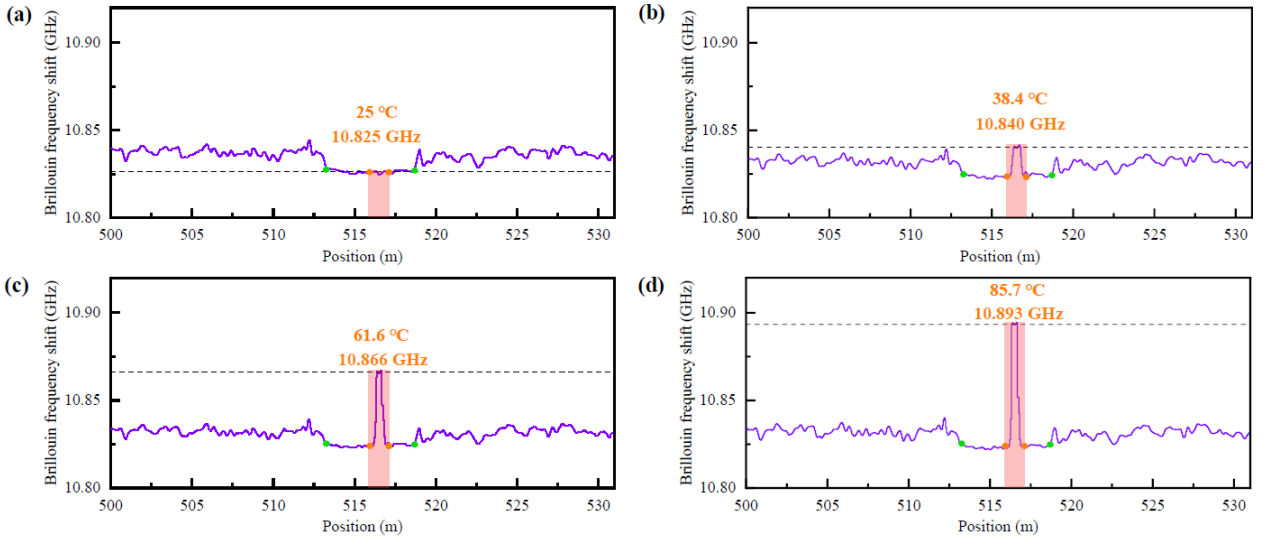

Fig. 7: Typical Brillouin frequency shifts around the fiber segment at (a) 25 °C, (b) 38.4 °C, (c) 61.6 °C and (d) 85.7 °C.

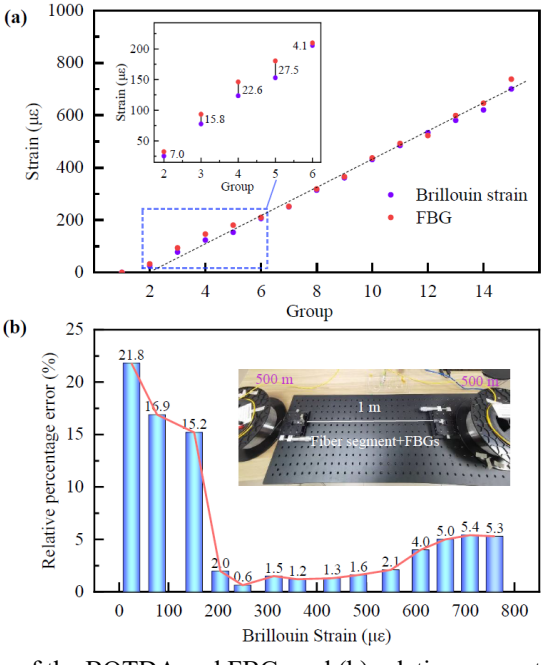

Fig. 8: (a) Strain response characteristics of the BOTDA and FBG, and (b) relative percentage error distribution as a function of the Brillouin strain.

approximately linear relationship, a notable discrepancy between the Brillouin strain and FBG strain is observed, particularly at low strain levels. When the FBG strain was below 200 με, the measured Brillouin strain was consistently lower, demonstrating reduced sensitivity relative to the FBG-based measurement. The strain difference reached a maximum of 27.5 με at an FBG strain of 180.3 με, as shown in the partially enlarged inset. The relative percentage error (*RPE*) was further employed to evaluate the Brillouin measurement error and was defined as the ratio of the absolute difference between the two strain measurements to the FBG strain. The *RPE* distribution as a function of Brillouin strain was shown in Fig. 8(b). The Brillouin strain showed a high accuracy with measurement errors within 2% at 200-500 με. At strains lower than 200 με, the measurement error peaked at 21.8%. According to the abrupt *RPE* change, the mutagenic point at 200 με was identified as the lower threshold for Brillouin strain measurements. When the strain exceeded 600 με, the measurement error rapidly increased from 5%, marking this point as the upper threshold for reliable Brillouin strain sensing. The errors in Brillouin strain exhibited pronounced nonlinearity and were inherently dependent on the strain level, primarily attributed to the reduced signal-to-noise ratio (SNR) in DPP-BOTDA[18] and fitting inaccuracies in the gain spectrum. While the incorporation of DPP technology in BOTDA improved spatial resolution on the order of cm from ~1 m of traditional BOTDA, it simultaneously compromises frequency shift accuracy due to signal-to-noise ratio (SNR) degradation caused by the subtraction of two time-domain signals. Therefore, the trade-off between spatial resolution and strain accuracy must be carefully considered in high-resolution Brillouin sensing applications.

5.2 Accuracy validation for the fidelity enhancing model

The fiber-optic gyro Coil-30 was selected to demonstrate the online transfer learning-based model for efficient fidelity enhancement of distributed Brillouin strain measurements. With the unwound fiber state serving as the zero-strain reference, the demodulated Brillouin strain exhibited an overall strain level close to 0 με, with no evident signal noise (Fig. 9(a)). Significant signal noise was introduced into the Brillouin strain data during the winding process of Coil-30, and the denoised Brillouin strain profile, comprising 150 measurement points, was designated as the source domain (Fig. 9(b)). The average strain in Coil-7 reached approximately 200 με. The FBG strain measurements were partitioned into the target domain $\boldsymbol{Y}_{tar-1}$ and validation domain (Fig. 9(c)), respectively. Using the fidelity enhancement model described in Section 3, the Brillouin strain was transferred from the source domain to the target domain through domain adaptation

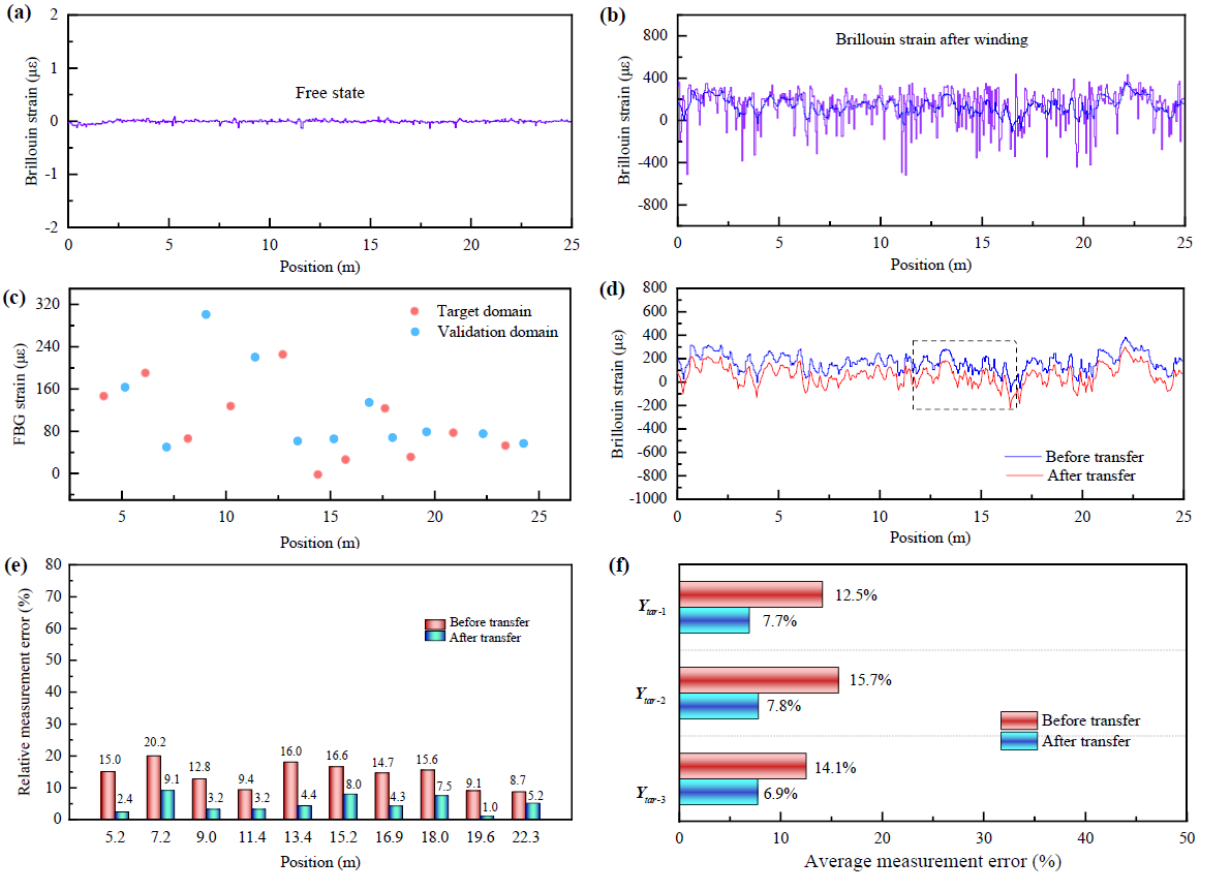

Fig. 9: Demodulated Brillouin strain in Coil-30 (a) at the fiber unwound state, (b) denoising Brillouin strain in the source domain, (c) FBG strain in the target domain and validation domain. (d) Brillouin strain and (e) relative percentage error before and after transfer with (f) Average measurement error with three target domains.

and weight-adaptive regression, as indicated by the red line in Fig. 9(d). From the local perspective, the strain curve not only shifted during domain adaptation but was also locally reshaped during weight-adaptive regression. The *RPE* of the Brillouin strain significantly decreased at all positions in the validation domain (Fig. 9(e)). The average measurement error Er decreased by 38.4%, from 12.5% to 7.7%, after transfer with $\boldsymbol{Y}_{tar-1}$ (Fig. 9(f)). Considering that target domain data are often limited in practical applications, a cross-validation strategy[40,41] was further employed to evaluate the fidelity enhancement model. With the same source domain, the average measurement error Er all decreased to a stable level of ~7% after transfer for target domain $\boldsymbol{Y}_{tar-1}$, $\boldsymbol{Y}_{tar-2}$ and $\boldsymbol{Y}_{tar-3}$. The Brillouin strain exhibited high fidelity after model-based transfer, as the alignment of the two domains effectively reduced the overall strain estimation error.

Fiber Coil-2500, with a total length of 2.5 km, was further employed to investigate the influence of the domain size ratio on strain fidelity enhancement performance. The target domain contained 35 FBG strain measurements, and the validation domain included 15 FBG strain measurements, both evenly distributed along the fiber coil (Fig. 10(a)). Due to the complex winding process of the structure, the Brillouin strain exhibited significant fluctuations within layers, generating distinct strain peaks at layer transition positions, as shown in Fig. 10(b). For long-range and complex strain distributions, the size of the source domain was progressively reduced from 50,000 to 25,000, 12,500, 7,000, 3,500, 1,750, and 875 by combining a thresholding filter with equally spaced sampling strategies (Fig. 10(c, d)), corresponding to domain size ratio SR of approximately 714, 357, 200, 100, 50, and 25 measurement points per FBG, respectively. Key strain features were effectively preserved even when the source domain size was reduced to 1.75% (875 points) of the original Brillouin strain data.

As shown in Fig. 11(a), as SR decreased from 714 to 25, all distributed strains were successfully transformed into point-wise strains, demonstrating that the model exhibits strong robustness in adapting to large domain sizes. Local strain distortions emerged when SR was less than or equal to 50, as indicated by the dashed lines. The measurement error *RPE* after transfer generally increased with decreasing SR (Fig. 11(b)). When SR was less than 50, the *RPE* after transfer slightly increased at some points in the validation domain, which was attributed to the overall transfer of the distributed strain. With the proposed fidelity enhancing model, the average measurement error Er in Coil-2500 (SR =714) decreased 79% from 10.5% to 2.2% compared to that before transfer (Fig. 11(c)). The first part of affine transformation in the model allowed source data curve to quickly approach the target data, and the average measurement error Er could quickly decreased 58% from 10.5% to 4.4% within 1.9 s (Fig. 11(c, d)). The transfer process could be accomplished online within 34.8 s (SR =714) for 2.5 km optical fiber coil, which was lower than a single measurement time of Brillouin strain of 52 s. Fiber-optic coils were often evaluated in the ground environment where computing resources were abundant. When measurement and enhancement are performed concurrently, the fast strain fidelity enhancement introduces no additional overhead in batch evaluation of optical fiber

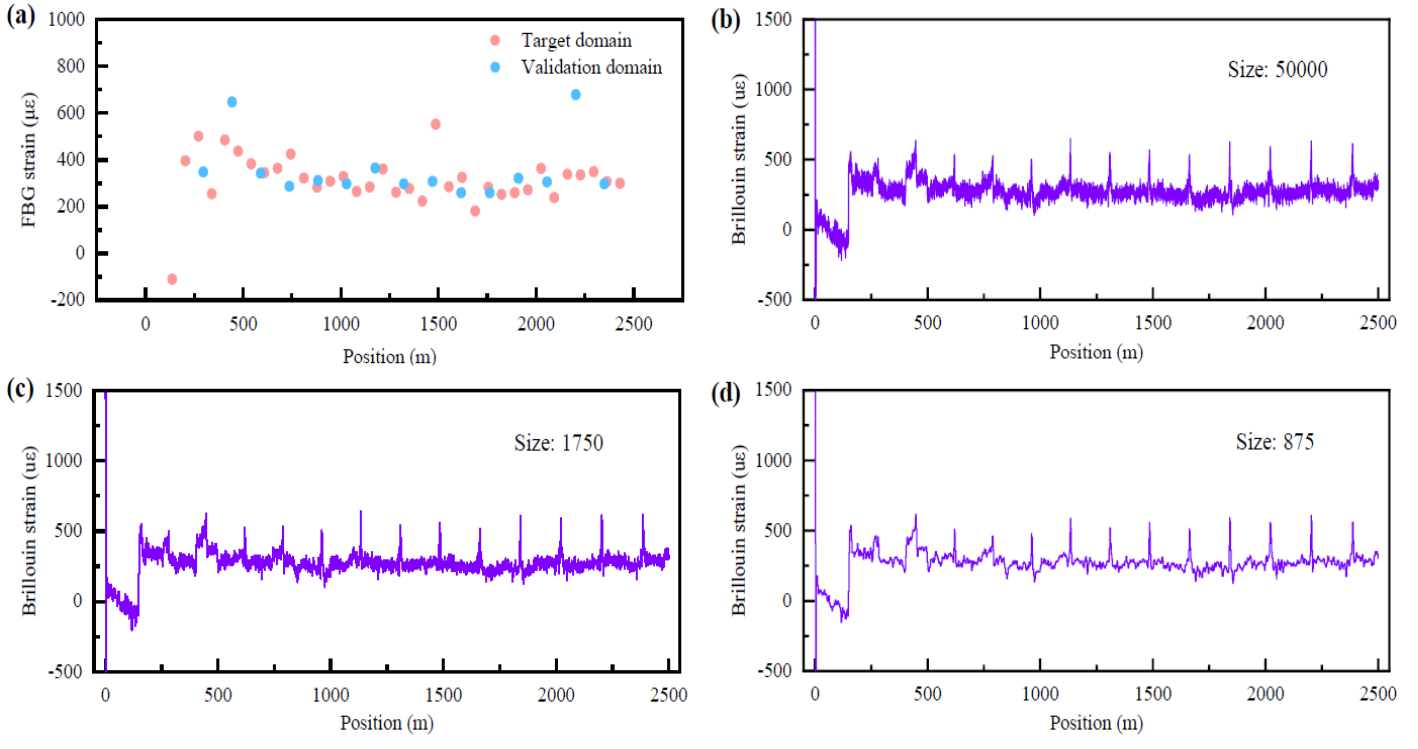

Fig. 10: (a) FBG strain in the target domain and validation domain of fiber Coil-2500. The Brillouin strain in the source domain with sizes of (a) 50000 (initial), (b) 1750 and (c) 875.

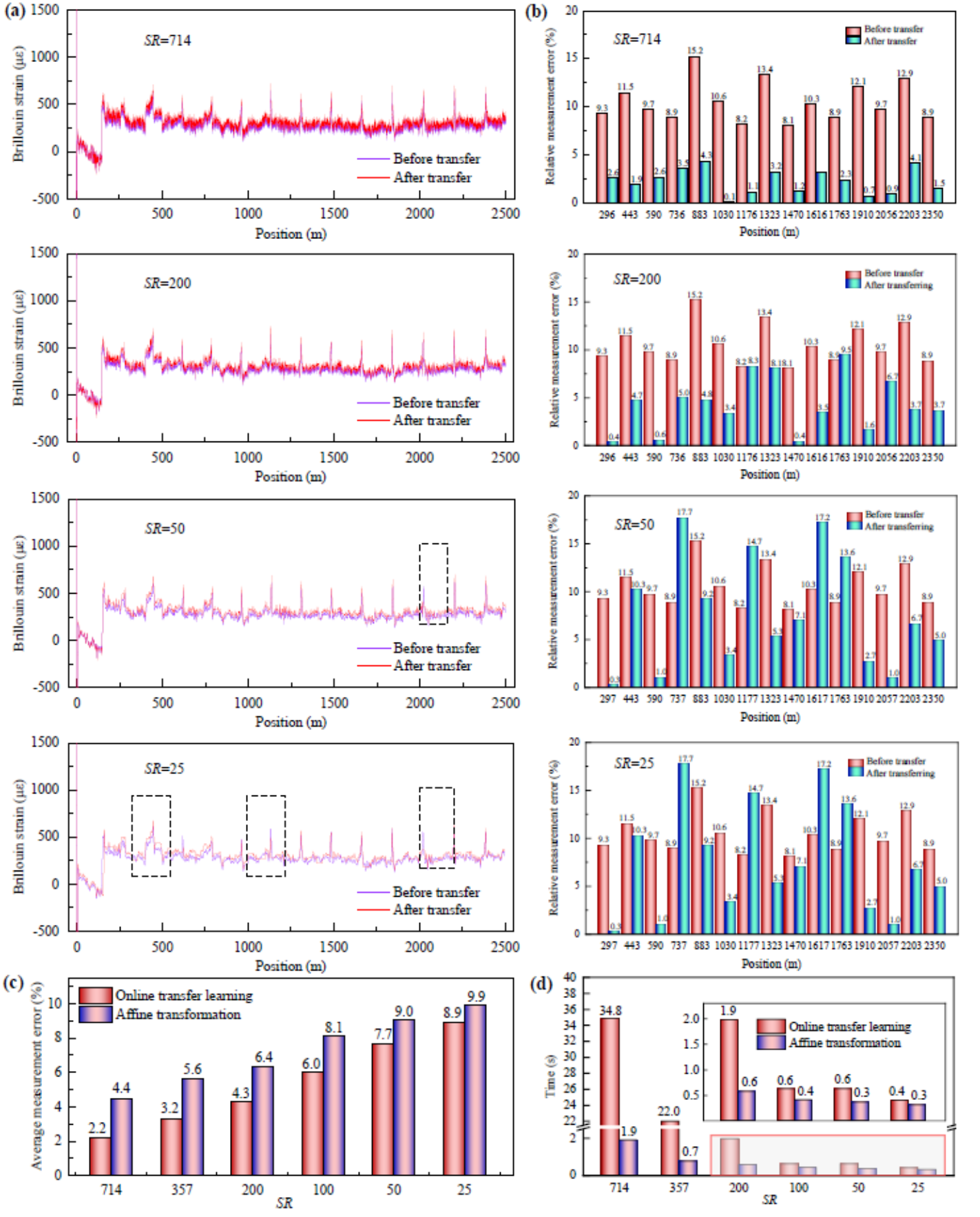

Fig. 11: Domain size ratio on enhancing performance of the strain fidelity (a) Brillouin strain and (b) measurement error RPE before and after transfer with of 714, 200, 50 and 25. (c) The average measurement error and (d) time consumption as a function of with the online transfer learning model or just affine transformation.

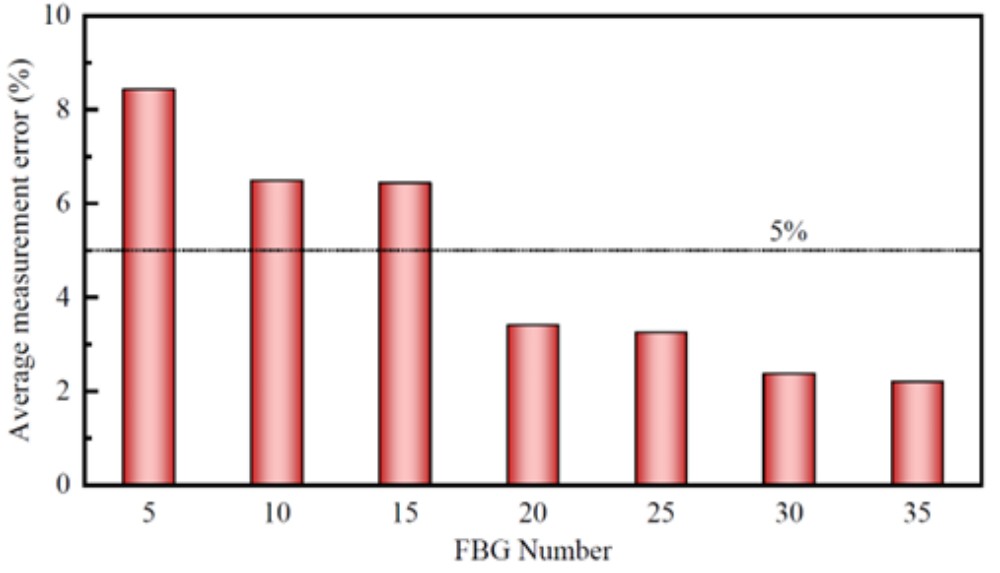

Fig. 12: The average measurement error for fiber coil-2500 as a function of randomly reduced FBG number.

coils. The time consumption exhibited an exponential decay with respect to the SR, primarily due to the algorithmic complexity of the weight-adaptive regression.

The feasibility of scaling the proposed approach to larger networks or more complex strain distribution patterns was demonstrated by systematically reducing the number of FBGs in the target domain from 35 to as few as 5. Using a fixed source domain (fiber coil-2500, size: 50,000), successful knowledge transfer was achieved across all target domains, resulting in enhanced strain measurement fidelity (Fig. 12).

Notably, even with a target domain as small as five FBGs, the average measurement error after transfer decreased by 20%. The online transfer model exhibited strong transferability across both uniform and non-uniform FBG distributions. This performance can be primarily attributed to the affine transformation, which initially aligned the distributed strain profile with point-wise strain measurements, followed by weight-adaptive regression that further refined the strain estimation in proximity to FBG locations. The proposed transfer framework demonstrated universality when applied to two distinct datasets with significant structural differences. When a 5% measurement error threshold was adopted, deploying 10 FBG measurement points per 1.25 km of optical fiber was found to be optimal for maximizing distributed strain fidelity. Using the current broadband light source (spectral bandwidth: 160 nm, Fig. 3) as the FBG demodulation scheme, approximately 50 gratings can be multiplexed in series on a single optical fiber simultaneously, with the measurement distance extendable up to 7.25 km. In the future, large-scale weak grating arrays fabricated via femtosecond laser inscription could be integrated with optical frequency domain reflectometry (OFDR) to enable multiplexing of thousands of FBGs in a scalable array configuration.[42] The proposed approach readily allows for extension of the measurement distance to the current upper limit of BOTDA, approximately 100 km.

5.3 Comparison with existing methods

Comparative experiments were conducted against traditional data fusion methods (IDW, GPR) and deep transfer learning techniques (DAN, JAN, and LSTM) to evaluate the performance of the proposed approach. For the fiber coil-2500 with 50000 distributed Brillouin strain (Fig. 13(a)) and 35 FBG strains (SR =714), the strain after enhancing with above existing methods were shown in Fig. 13. Using traditional data fusion methods (Fig. 13(b, c)), the strain distribution pattern remained unchanged after simple weighted fusion or Gaussian process regression of distributed and point strain measurements, leading to an increase in the average measurement error by 10.8% and 12.6%, respectively (Fig. 13(h)). Due to the lack of consideration for the overall data structure, these fusion approaches struggled to effectively reconcile two datasets exhibiting a significant discrepancy. When applying advanced transfer learning techniques (Fig. 13(d, e, f)), excessive alignment occurred, leading to a weakening or even severe loss of the source domain's distribution characteristics after transfer. Existing deep learning techniques of DAN, JAN and LSTM struggled to adapt to scenarios with significant size discrepancies between the source and target domains. In contrast, the proposed online transfer learning-based fidelity enhancement model demonstrated superior performance, reducing the average measurement error significantly from 10.5% to 2.2% compared to pre-transfer results (Fig. 13(g)). This approach proves particularly suitable for cases involving large data gaps, substantial domain size differences, or severely limited availability of accurate strain data.

This model utilizes only the measured distributed strain and point strain as inputs, with their complex implicit correlations dynamically established during the learning process. A small number of accurate data points are sufficient to transfer the distributed strain from low to high fidelity. The approach does not rely on costly data labeling or extensive

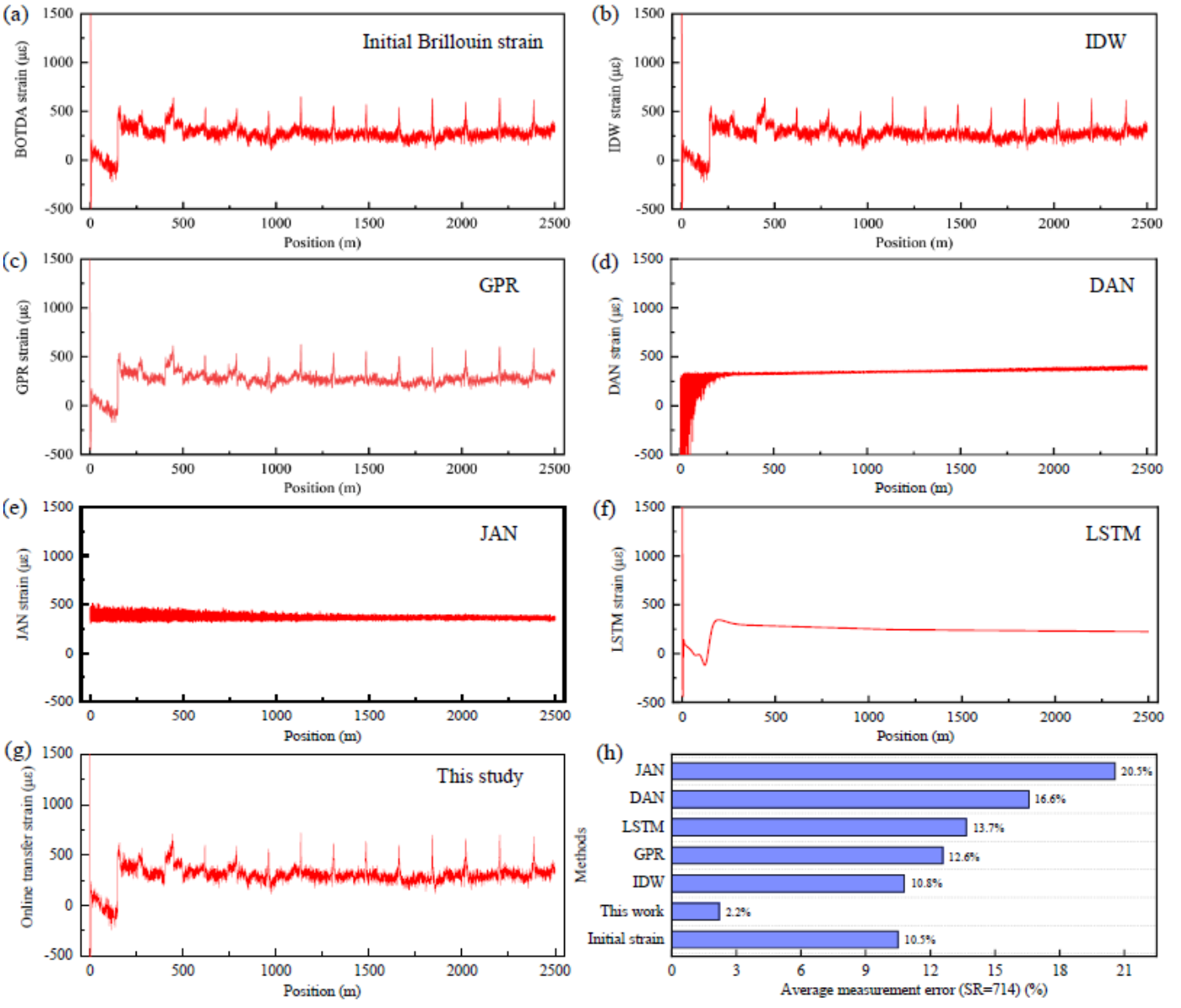

Fig. 13: Comparative with existing methods. (a) Initial Brillouin strain, and the enhanced strain by (b) IDW, (c) GPR, (d) DAN, (e) JAN, (f) LSTM, and (g) the approach in this work. (h) The average measurement error comparison of above methods.

historical datasets, offering greater generalizability than existing transfer learning methods[28] in scenarios involving variable correlations. The distributed strain sensor network integrates the advantages of both BOTDA and FBG mechanisms within the same FUT. By combining distributed Raman temperature measurement technology,[43] the sensing capacity of high-fidelity distributed strain will enable the sensor network to play an irreplaceable role in long-distance underwater communication, fatigue monitoring of aerospace structures, geological disaster early warning, bridge or dam monitoring. In this work, the online transfer learning based fidelity enhancing model relies on FBG in FUT as an accurate strain reference, which may bring inconvenience to some functional optical fiber structure. The time consumption can be further optimized by introducing parallelization, edge computing, or hardware acceleration strategies for field deployment in time-sensitive applications. In the future work, the error distribution characteristics of Brillouin strain can be further studied and memorized for direct measurement error compensation of BOTDA.

6. Conclusion

A high-fidelity distributed strain sensing technique was proposed and demonstrated by optically fusing DPP-BOTDA and FBG mechanisms into the same fiber and assisting with an online transfer learning based fidelity enhancing model. In addition to refractive index modulation depth, the opposite propagation direction of the continuous probe light and the backscattered light from FBGs was another basis for the optical fusion of the BOTDA and FBG mechanisms. The sensor network was highly accurate, nondestructive, easy to wire and low-cost, which was widely applicable in long-

distance underwater communication, fatigue monitoring of aerospace structures, geological disaster early warning.

Brillouin strain errors at high spatial-resolution sensing exhibited evident nonlinearity and were also related to the strain itself due to the reduced SNR in DPP-BOTDA and gain spectrum fitting error. The Brillouin strain showed measurement errors within 2% at 200-500 με, but the measurement error was the largest reaching 21.8% at strains lower than 200 με. This should be considered during the safety assessment of a precision optical structure. A new online transfer learning model was proposed for enhancing distributed strain fidelity by combining affine transformation and adaptive weighting, which addressed the challenge of mapping strain instance vectors between the source domain and target domain with large data gaps and significant size differences. The average measurement error of distributed strain in 2.5 km was decreased 79% from 10.5% to 2.2% within 34.8 s, and the model could scale to larger networks up to 100 km theoretically. For each measurement, only a small amount of reliable strain data was necessary to improve the fidelity level of the distributed strain, without the need for a large amount of labeled data and historical data to establish complex implicit correlations between the distributed and point strains.

Acknowledgments

This work was supported by the Natural Science Foundation of China (Nos. 52305553, U2241247), Natural Science Basic Research Project of Shaanxi Province (No. 2025JC-YBMS-381), Fundamental Research Funds for the Central Universities (No. ZYTS25050).

Conflict of Interest

The authors declare no conflict of interest.

Supporting Information

Not applicable.

CRediT Statement

Yongxi He: Conceptualization, Methodology, Writing - Original draft. **Ye Liang:** Methodology, Data curation. **Wenjie Gao:** Visualization, Software. **Xuechao Duan:** Funding acquisition, Supervision. **Yongqiang Guan:** Writing - Review & editing.

References

[1] L. A. Levin, D. J. Amon, H. Lily, Challenges to the sustainability of deep-seabed mining, *Nature Sustainability*, 2020, **3**, 784-94, doi: 10.1038/s41893-020-0558-x.

[2] R. K. Singh, R. G. Sangeetha, Review of EMC standards for underwater vehicles, *Results in Engineering*, 2024, **24**, 103068, doi: 10.1016/j.rineng.2024.103068.

[3] S. Fan, K. Chan, C. K. H. Chin, Motion analysis of an autonomous underwater vehicle tethered with an optical fiber for real-time surveillance, *IEEE Journal of Oceanic Engineering*, 2020, **46**, 434-446, doi: 10.1109/JOE.2020.2986876.

[4] D. Guang, X. Sun, J. Shi, X. Wu, C. Zuo, P. Zhu, B. Yu, High-performance interferometric fiber optic hydrophone based on mandrel structure in deep sea, *IEEE Transactions on Instrumentation and Measurement*, 2025, **74**, 7010509, doi: 10.1109/TIM.2025.3581660.

[5] Z. Zhan, M. Cantono, V. Kamalov, A. Mecozzi, R. Müller, S. Yin, J. C. Castellanos, Optical polarization ‐ based seismic and water wave sensing on transoceanic cables, *Science*, 2021, **371**, 931-936, doi: 10.1126/science.abe6648.

[6] Y. Guo, J. M. Marin, I. Ashry, A. Trichili, M.-N. Havlik, T. K. Ng, C. M. Duarte, B. S. Ooi, Submarine optical fiber communication provides an unrealized deep-sea observation network, *Scientific Reports*, 2023, **13**, 15412, doi: 10.1038/s41598-023-42748-0.

[7] Q. Liu, J. Bao, Y. Shao, L. Zheng, H. Xu, Dynamic modeling and underwater configuration analysis of fiber optic cable for UUV-launched UAV, *Ocean Engineering*, 2024, **303**, 117774, doi: 10.1016/j.oceaneng.2024.117774.

[8] M. Jia, G. Yang, Research of optical fiber coil winding model based on large-deformation theory of elasticity and its application, *Chinese Journal of Aeronautics*, 2011, **24**, 640-647, doi: 10.1016/s1000-9361(11)60075-7.

[9] J. Pillon, F. Louf, H. Boiron, M. Rattier, E. Peter, P.-A. Boucard, H. C. Lefèvre, Thermomechanical analysis of the effects of homogeneous thermal field induced in the sensing coil of a fiber-optic gyroscope, *Finite Elements in Analysis and Design*, 2022, **212**, 103826, doi: 10.1016/j.finel.2022.103826.

[10] Q. Liu, T. Tokunaga, Z. He, Ultra-high-resolution large-dynamic-range optical fiber static strain sensor using Pound ‐ Drever ‐ Hall technique, *Optics Letters*, 2011, **36**, 4044-4046.

[11] Y. Yan, H. Zheng, Z. Zhao, C. Guo, X. Wu, J. Hu, A. P. T. Lau, C. Lu, Distributed optical fiber sensing assisted by optical communication techniques, *Journal of Lightwave Technology*, 2021, **39**, 3654-3670, doi: 10.1109/JLT.2021.3057670.

[12] M. A. Soto, J. A. Ramírez, L. Thévenaz, Intensifying the response of distributed optical fibre sensors using 2D and 3D image restoration, *Nature Communications*, 2016, **7**, 10870, doi: 10.1038/ncomms10870.

[13], R. D. Prasad, N. R. Prasad, N. Prasad, S. R. Prasad, R. S. Prasad, R. B. Prasad, R. R. Prasad, R. G. Prasad, C. B. Desai, A. K. Vaidya, Y. I. Shaikh, G. M. Nazeruddin, V. Shaikh, R. S. Pande, P. M. Mamidpelliwar, R. N. Deshmukh, V. N. Patil, A. Samant, C. Chiplunkar, Z. Guo, P. Sarvalkar, A. A. Ramteke, A. D. Shaikh, A review on scattering techniques for analysis of nanomaterials and biomaterials, *Engineered Science*, 2024, **33**, 1332, doi: 10.30919/es1332.

[14] W. Zuo, H. Zhou, Y. Qiao, Multi-band chirped pulse based Φ-OTDR for fading suppression and high spatial resolution, *Optics and Lasers in Engineering*, 2025, **186**, 108833, doi: 10.1016/j.optlaseng.2025.108833.
[15] Y. Zhang, Y. Lu, Z. Zhang, J. Wang, C. He, T. Wu, Noise reduction by Brillouin spectrum reassembly in Brillouin optical time domain sensors, *Optics and Lasers in Engineering*, 2020, **125**, 105865, doi: 10.1016/j.optlaseng.2019.105865.
[16] W. Li, X. Bao, Y. Li, L. Chen, Differential pulse-width pair BOTDA for high spatial resolution sensing, *Optics Express*, 2008, **16**, 21616, doi: 10.1364/oe.16.021616.
[17] X. Ge, T. Wang, Q. Zhang, J. Peng, Y. Zhu, Y. Zhang, J. Zhang, L. Qiao, Zhang M. Improving BOTDA performance based on differential pulse width pair and FFDNet, *IEEE Sensors Journal*, 2024, **24**, 16137-44, doi: 10.1109/JSEN.2024.3382683.
[18] S. Li, Z. Zhao, C. Zhao, H. Wu, C. Lu, M. Tang, Improving the spatial resolution of a BOTDA sensor using deconvolution algorithm, *Journal of Lightwave Technology*, 2024, **39**,2215-22, doi: 10.1109/JLT.2020.3047504.
[19] R. Liang, C. Huang, C. Zhang, B. Li, S. Saydam, I. Canbulat, Data diagram design and data management for visualisation and analytics fusion in the mining industry, *Engineered Science*, 2023, **32**, 1036, doi: 10.30919/es1036.
[20] T. Chompookham, K. Tongnate, S. Phiphiphatphaisit, S. Lata, N. Angkawisittpan, S. Sultornsanee, The feature fusion multi-conv networks using best feature selection for face recognition, *Engineered Science*, 2025, **37**, 1805, doi: 10.30919/es1805.
[21] H. Ye, W. Zhao, Multi-strategy fusion improves time optimal trajectory planning of particle swarm optimization algorithm, *ES General*, 2025, **8**, 1515, doi: 10.30919/esg1515.
[22] S.-S. Jin, S. T. Kim, Y.-H. Park, Combining point and distributed strain sensor for complementary data-fusion: a multi-fidelity approach, *Mechanical Systems and Signal Processing*, 2021, **157**, 107725, doi: 10.1016/j.ymssp.2021.107725.
[23] D. Zhang, Z. Li, Y. Duan, L. Yang, H. Liu, FBG and BOTDA based monitoring of mine pressure under remaining coal pillars using physical modeling, *Sensors*, 2024, **24**, 7037, doi: 10.3390/s24217037.
[24] A. Zrelli, Simultaneous monitoring of temperature, pressure, and strain through Brillouin sensors and a hybrid BOTDA/FBG for disasters detection systems, *IET Communications*, 2019, **13**, 3012-3019, doi: 10.1049/iet-com.2018.5260.
[25] Z. Zhou, J. He, J. Ou, Integrated optical fiber sensing system by combing large-scale distributed BOTDA/R and localized FBGs, *International Journal of Distributed Sensor Networks*, 2012, **8**, 804394, doi: 10.1155/2012/804394.
[26] Y. He, W. Gao, Y. Liang, S. Wang, Y. Zhang, X. Duan, Online transfer assisted LSTM model for fast nonlinear strain error compensation of BOTDA sensing, *Optics & Laser Technology*, 2025, **190**, 113233, doi: 10.1016/j.optlastec.2025.113233.
[27] M. S. Iqbal, S. Munawar, M. Adnan, S. E. G. Mohamed, An efficient approach for electricity theft detection based on transfer learning in temporal sequence, *Results in Engineering*, 2025, **26**, 105125, doi: 10.1016/j.rineng.2025.105125.
[28] Z. Zhao, L. Alzubaidi, J. Zhang, Y. Duan, Y. Gu, A comparison review of transfer learning and self-supervised learning: Definitions, applications, advantages and limitations, *Expert Systems with Applications*, 2024, **242**, 122807, doi: 10.1016/j.eswa.2023.122807.
[29] Q. Huang, Y. Bao, J. Sun, C. Huang, Distributed Brillouin optical fiber sensors assisted by first-order Raman amplification with window functions, *Optics and Lasers in Engineering*, 2023, **164**, 107504, doi: 10.1016/j.optlaseng.2023.107504.
[30] J. Wang, R. Tang, L. Zhang, Distributed measurement based on sparse spectra of Brillouin optical fiber sensors in IoT, *IEEE Transactions on Instrumentation and Measurement*, 2024, **73**, 7009108, doi: 10.1109/TIM.2024.3480221.
[31] B. Wang, L. Wang, N. Guo, Z. Zhao, C. Yu, C. Lu, Deep neural networks assisted BOTDA for simultaneous temperature and strain measurement with enhanced accuracy, *Optics Express*, 2019, **27**, 2530, doi: 10.1364/oe.27.002530.
[32] M. Manconi, S. P. G. F. Moonen, A full computational framework for the temperature analysis of a flax-reinforced composite footbridge with field monitoring validation, *Results in Engineering*, 2024, **23**, 102718, doi: 10.1016/j.rineng.2024.102718.
[33] K. P. Chen, P. R. Herman, Photosensitization of standard fibers with deep UV laser radiation, *Journal of Lightwave Technology*, 2003, **21**, 1958-1968, doi: 10.1109/JLT.2003.815643.
[34] A. A. Amin, M. Sajid Iqbal, M. Hamza Shahbaz, Development of intelligent fault-tolerant control systems with machine learning, deep learning, and transfer learning algorithms: a review, *Expert Systems with Applications*, 2024, **238**, 121956, doi: 10.1016/j.eswa.2023.121956.
[35] D. Tang, X. Yang, X. Wang, Improving the transferability of the crash prediction model using the TrAdaBoost.R2 algorithm, *Accident Analysis & Prevention*, 2020, **141**, 105551, doi: 10.1016/j.aap.2020.105551.
[36] K. Wang, J. Lu, A. Liu, Y. Song, L. Xiong, G. Zhang, Elastic gradient boosting decision tree with adaptive iterations for concept drift adaptation, *Neurocomputing*, 2022, **491**, 288-304, doi: 10.1016/j.neucom.2022.03.038.
[37] K. Yuan, W. Xu, W. Li, W. Ding, An incremental learning mechanism for object classification based on progressive fuzzy three-way concept, *Information Sciences*, 2022, **584**, 127-147, doi: 10.1016/j.ins.2021.10.058.
[38] Q. Liang, S. Nittel, J. C. Whittier, S. de Bruin, Real-time inverse distance weighting interpolation for streaming sensor data,

Transactions in GIS, 2018, **22**, 1179-1204, doi: 10.1111/tgis.12458.
[39] J. C. Briñez-de León, H. López-Osorio, M. Rico-García, H. Fandiño-Toro, Deep learning as a powerful tool in digital photoelasticity: Developments, challenges, and implementation, *Optics and Lasers in Engineering*, 2024, **180**, 108274, doi: 10.1016/j.optlaseng.2024.108274.
[40] X. Zhang, H. Liu, Linear programming-based reconstruction algorithm for limited angular sparse-view tomography, *Optics and Lasers in Engineering*, 2021, **140**, 106524, doi: 10.1016/j.optlaseng.2020.106524.
[41] J. Paredes, D. Chávez, R. Isa-Jara, D. Vargas, A hybrid machine learning algorithm approach to predictive maintenance tasks: a comparison with machine learning algorithms, *Results in Engineering*, 2025, **26**, 105137, doi: 10.1016/j.rineng.2025.105137.
[42] B. Chen, A. Li, J. Yang, D. Zhang, J. Li, M. Zhang, Q. Cheng, J. Zhu, Y. Li, Real-time monitoring of strain processes with large-range and high-spatial resolution using the method of weak reflection FBG measurement based on OFDR, *IEEE Transactions on Instrumentation and Measurement*, 2023, **73**, 3000111.
[43] J. Li, M. Zhang, Physics and applications of Raman distributed optical fiber sensing, *Light*: *Science & Applications*, 2022, **11**, 128, doi: 10.1038/s41377-022-00811-x.